



Rapid hydrogen adsorption-desorption at sulfur sites via an interstitial carbon strategy for efficient HER on MoS₂

Qingqing Zhou ^a, Zhongyuan Wang ^a, Huadong Yuan ^c, Jiade Wang ^{a,b,*}, Hao Hu ^a

^a College of Environment, Zhejiang University of Technology, Hangzhou 310012, PR China

^b Key Laboratory of Microbial Technology for Industrial Pollution Control of Zhejiang Province, Hangzhou 310012, PR China

^c College of Material Science and Engineering, Zhejiang University of Technology, Hangzhou 310012, PR China



ARTICLE INFO

Keywords:

Hydrogen evolution reactions
Unsaturated electronic structure
Molybdenum disulfide
Interstitial atomic carbon

ABSTRACT

Molybdenum disulfide (MoS₂), a noble-free material with plentiful unsaturated active edge sites, is expected to replace platinum catalysts for commercial electrocatalytic hydrogen production. However, efficient hydrogen adsorption-desorption processes on sulfur sites with full electron configuration still remain a challenge. Here, vertically oriented self-assembled metallic MoS₂ nanospheres anchored by interstitial atomic carbon (C_{ia}-MoS₂) are proposed to achieve a rapid hydrogen adsorption-desorption process. In 0.5 M H₂SO₄ solution, C_{ia}-MoS₂ exhibits fast kinetics (Tafel slope of 45 mV dec⁻¹ and overpotential of 87 mV at 10 mA cm⁻²), as well as a long-term durability over 72 h. As confirmed from X-ray absorption fine spectroscopy and density functional calculations, C_{ia} significantly optimizes the overall HER performance by reconfiguring the charge landscape and re-splitting the energy level of surface S moiety, which provides a universal strategy for fabricating stable unsaturated 2D catalysts toward HER.

1. Introduction

Electrocatalytic water splitting has attracted continuous attention in the production of green hydrogen due to its carbon-free emission and high purity [1,2]. Platinum is considered to be the most favorable catalyst for hydrogen generation, however, not convenient for universal utilization due to its costliness [3,4]. An ideal electrocatalyst for the hydrogen evolution reaction (HER) should be free of noble and possess abundant potential active sites, high current efficiency, and reliable stability.

Molybdenum disulfide (MoS₂), a typical transition metal dichalcogenide (TMD), has long been considered a suitable candidate for universal application due to its tunable lamellar structure and “platinum-like behavior” [5,6]. Such characteristic is attributed to the near thermoneutral hydrogen-binding energy at the MoS₂ edges (Mo-edge ($\Delta G_{H^*} \approx 0.06$ eV) and S-edges ($\Delta G_{H^*} \approx -0.45$ eV)), endowed with higher potential energy and HER reactivity [7,8]. However, surface S layers with fully electronic structures possess poor charge transfer kinetics and are unable to hydrogenate ($\Delta G_{H^*} \approx 1.92$ eV), thereby inappropriate for H₂O activation and desorption [9–11]. The sluggish water dissociation process (Volmer step) severely hampers the formation of adsorbed hydrogen atoms and the subsequent hydrogen evolution process

(Heyrovsky or Tafel step). For this sake, d-electron-rich transition metal atoms (e.g., Co, Ni, Fe) were introduced into MoS₂ to optimize the electron structure, and its effect on HER activity has been verified by density functional theory (DFT) calculations and extensive research [12–15]. However, transition metal atoms are mainly combined with MoS₂ by replacing homogeneous host atoms [16–18]. A general way for controllable tuning the electronic structure and geometric configuration of MoS₂ toward efficient HER is still missing.

Atomically carbon placed in crystal subsurface has been found to be efficient for enhancing both surface catalytic activity and low-coordinated site stability for metal catalysts [19,20]. However, carbon atoms located on the surface of the catalyst may segregate into graphitic nanostructures as the catalytic reaction proceeds [21]. Therefore, space confinement of atomic carbon in the crystal interstice is a promising strategy to tune surface catalytic activity and unsaturated catalytic systems stability, which is little reported on MoS₂ catalyst for HER application. Here, a versatile method of interstitial carbon (C_{ia}) was proposed to promote the efficiency of HER of MoS₂, more specifically, C_{ia} is spatially confined in the MoS₂ subsurface interstice. Meanwhile, MoS₂ displaced by cobalt atoms (Co-MoS₂) and pristine MoS₂ were used as counterparts to understand the effect of the mode/structure of dopants on the HER catalytic reaction. Electrochemical tests in acidic media

* Corresponding author.

E-mail address: jdwang@zjut.edu.cn (J. Wang).

show that $\text{C}_{\text{ia}}\text{-MoS}_2$ has a significantly optimized charge transfer process and hydrogen binding capacity with the lowest Tafel slope of 45 mV dec⁻¹, compared with 95 and 238 mV dec⁻¹ of Co-MoS₂ and MoS₂. Long-term stability tests showed that $\text{C}_{\text{ia}}\text{-MoS}_2$ retained its morphological and structural integrity after 72 h of continuous H₂ generation. The high electronegativity difference between C_{ia} and Mo endows the active sites with excellent durability than that of Co-MoS₂. X-ray absorption spectroscopy and DFT calculations were further conducted to reveal the modulation patterns of C_{ia} and Co sites on the ability of MoS₂ for HER catalysis. It is found that the C_{ia}-induced re-splitting of the S energy level can effectively tune the adsorption of hydrogen species on the S moiety, enabling a fast hydrogen adsorption-desorption process. Our work not only proposes interstitial nonmetal single atoms as efficient charge transport media in 2D-MoS₂ catalysts but also reveals the relationship of two atomic-level dopants to the electronic structure and HER response of MoS₂.

2. Experimental section

2.1. Fabrication of $\text{C}_{\text{ia}}\text{-MoS}_2$ nanosheets

Interstitial atomic carbon-doped MoS₂ nanosheets ($\text{C}_{\text{ia}}\text{-MoS}_2$) was synthesized by a simple hydrothermal method. 40.3 mg of sodium molybdate dihydrate ($\text{Na}_2\text{MoO}_4 \cdot 2\text{H}_2\text{O}$, ACS Grade, Sigma Aldrich) and 101 mg of L-cysteine ($\text{C}_3\text{H}_7\text{NO}_2\text{S}$, ACS Grade, Sigma Aldrich) were dissolved in 30 mL of Millipore water (18.2 MΩ cm) under vigorous stirring until a homogeneous solution was achieved. The mixture solution was then transferred into a 100 mL Teflon-lined autoclave and maintained at 220 °C for 18 h. The product was washed several times with ethanol and water to remove residual ions. Then, the collected powder was vacuum-dried at 80 °C overnight. The final products were prepared into black ink for electrochemical measurements.

2.2. HER electrochemical evaluation

The HER electrochemical performance was evaluated in 0.5 M H₂SO₄ using a three-electrode system. The glassy carbon electrode coated with the catalysts, the standard saturated Ag/AgCl electrode, and the graphite rod were served as working electrode, the reference electrode, and the counter electrode, respectively. All potentials were converted to RHE with the following equation: $E \text{ (vs. RHE)} = E \text{ (vs. Ag/AgCl)} + 0.197 + 0.059 \times \text{pH}$. All data presented were IR-corrected, where the solution resistances were obtained by testing EIS in the frequency range of 0.1–10⁴ Hz. The LSV experiment was conducted with a scan rate of 2 mV s⁻¹. Experimental details including the synthesis of control samples, electrochemical evaluation in a three-electrode system, material characterization, and DFT calculations can be found in the [Experimental Section of the Supporting Information](#).

3. Results and discussion

3.1. Synthesis and crystal characterization

The electrocatalysts were synthesized by a simple hydrothermal process at 220 °C for 18 h. Following the schematic diagram in Fig. 1a, $\text{C}_{\text{ia}}\text{-MoS}_2$ was prepared from a mixture of sodium molybdate and L-cysteine at a molar ratio of 1:5. Combing the LSV, powder X-ray diffraction (XRD), and Raman analysis (Fig. S1) of samples under different ratios, it was confirmed that the carbon doping content and catalytic performance are well controlled by adjusting the stoichiometric of the mixture (Table S1). Using thiourea to provide S source for Co-MoS₂ and MoS₂ catalysts and see Methods for the detailed synthesis process. Scanning electron microscopy (SEM) and transmission electron microscopy (TEM) are used to observe detailed nanosheet structures of the three catalysts (Figs. S2–S4). Apparently, different precursor

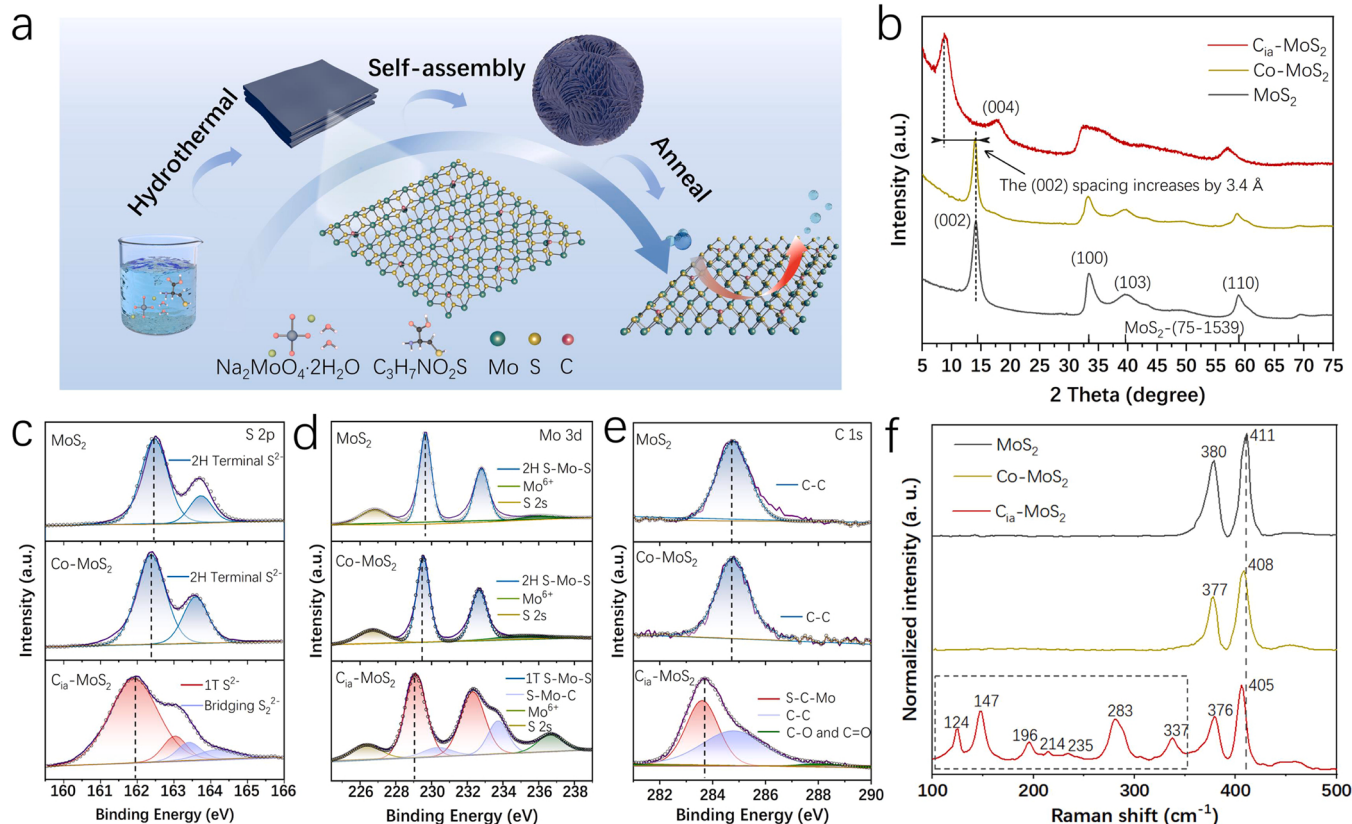


Fig. 1. (a) Schematic diagram of the synthesis of $\text{C}_{\text{ia}}\text{-MoS}_2$. (b) XRD patterns, (c) S 2p XPS spectra, (d) Mo 3d XPS spectra, (e) C 1s XPS spectra, and (f) Raman spectra of MoS₂, Co-MoS₂, and $\text{C}_{\text{ia}}\text{-MoS}_2$.

environments and nucleation processes provide constraints for the anisotropic growth of MoS₂ nanosheets to obtain different nanostructures.

XRD spectra in Fig. 1b shows that the as-synthesized MoS₂ samples have well-defined crystal structures, without any crystalline C- and Co-containing species. The diffraction peaks of MoS₂ and Co-MoS₂, which are located at 14.2°, 33.2°, and 58.9°, were indexed as the (002), (100), and (110) peaks of 2 H-phase MoS₂ (JCPDS No.75-1539). Furthermore, the (002) peak of C_{ia}-MoS₂ is negatively shifted by about 5°, corresponding to the expansion of the interlayer spacing to 0.96 Å. The new peak exposed at ~17.85° can be attributed to (004) peak of 1 T C_{ia}-MoS₂. The grain size, microstrain, lattice spacing, and crystal volume of C_{ia}-MoS₂, Co-MoS₂, and MoS₂ are summarized in Table S2. Interestingly, microstrains of the exposed typical planes on C_{ia}-MoS₂ were all significantly enhanced, corresponding to an expansion of the crystal bulk from 105.7 Å³ to 110.3 Å³, which was attributed to the entry of C_{ia} into the MoS₂ lattice. In contrast, it was speculated that the bulk volume of Co-MoS₂ decreased to 103.5 Å³ due to the substitution of Mo atoms by Co, which has a smaller radius.

Fig. 1(c, d) shows a comparison of the high-resolution S 2p and Mo 3d X-ray photoelectron spectroscopy (XPS) results of the as-synthesized C_{ia}-MoS₂, Co-MoS₂, and MoS₂ samples. The measured S 2p3/2 and Mo 3d5/2 binding energies of C_{ia}-MoS₂ were both 0.6 eV lower than those of Co-MoS₂ and MoS₂, which is a typical identification for 2 H-1 T phase transition [22,23]. It was inferred that the lowest chemical valences of S and Mo in the 1 T phase are due to the increased electron cloud density of the whole system as the electrophilic S atomic layer slips. In Fig. 1c, two distinct peaks at ~163.4 and 164.1 eV were assigned to the shared bridging disulfide (S₂²⁻) ligands with higher chemical states and reactivities [24]. Strikingly, the new doublet at ~230.3 and 233.7 eV in Fig. 1d suggests that the chemical state of Mo was influenced by C intercalation and forms the S-Mo-C bond. Subsequently, the C 1s

spectrum of C_{ia}-MoS₂ (Fig. 1e) exhibits asymmetry, where the main peak is negatively shifted due to C_{ia} attracting surrounding electrons, and the minor peak may be caused by sample oxidation [25]. The Co 2p spectra are shown in Fig. S5. Obviously, Co hardly disturbs the chemical composition of MoS₂, which is consistent with the XRD analysis results. Next, ultraviolet photoelectron spectroscopy (UPS) was employed to obtain their work function, which follow the formula ($\Phi = h\nu - (E_{\text{Cut off}} - E_{\text{Fermi}})$), where $h\nu$ is 21.22 eV and E_{Fermi} is 0 eV. As shown in Fig. S6, C_{ia}-MoS₂ exhibits the smallest work function of 3.89 eV, corresponding to the lowest energetic barrier for electrons migration, resulting in efficient hydrogen adsorption behavior during HER process [26]. Raman spectra comparison (Fig. 1f) was collected to reveal the structural symmetry difference of the as-synthesized MoS₂. Co-MoS₂ shows two prominent Raman bands at 377 and 408 cm⁻¹, as a result of in-plane (E_{2g}¹) and out-of-plane (A_{1g}) Mo-S phonon modes of 2 H phase vibrational configurations [25]. In contrast, the existence of new peaks for C_{ia}-MoS₂ at 124, 147, 196, 214, 235, 283, and 337 cm⁻¹ were ascribed to 1 T MoS₂ longitudinal phonon vibration [27,28] and accompanied by significantly weakened 2 H-MoS₂ characteristic peak intensities (E_{2g}¹ and A_{1g}).

TEM and HAADF imaging were further performed to observe the morphology details of the as-synthesized MoS₂ catalysts. As shown, MoS₂ clusters are formed by stacking small-scale nanosheets (Fig. 2a), while Co-MoS₂ shows a distinct core accompanied by larger and ductile nanosheets (Fig. 2e). Surprisingly, C_{ia}-MoS₂ is a self-assembly central radial spherical nanostructure with vertical nanosheets that fully expose the active edges (Fig. 2i). The energy-dispersive X-ray spectroscopy (EDX) analysis patterns (Fig. 2c, g, k) show that all the elements were homogeneously dispersed in the as-synthesized samples. The high-resolution TEM (HRTEM) images in Fig. 2b and Fig. 2f clearly show the (100) plane lattice fringes, along with the selected area electron diffraction (SAED) patterns. The HRTEM images in Fig. 2j and Fig. 2l show the (002) plane lattice fringes, along with the SAED patterns. The corresponding line intensity analysis (Fig. 2d, h, l) shows the periodic intensity variation of the corresponding lattice fringes, indicating the single-crystalline nature of the samples.

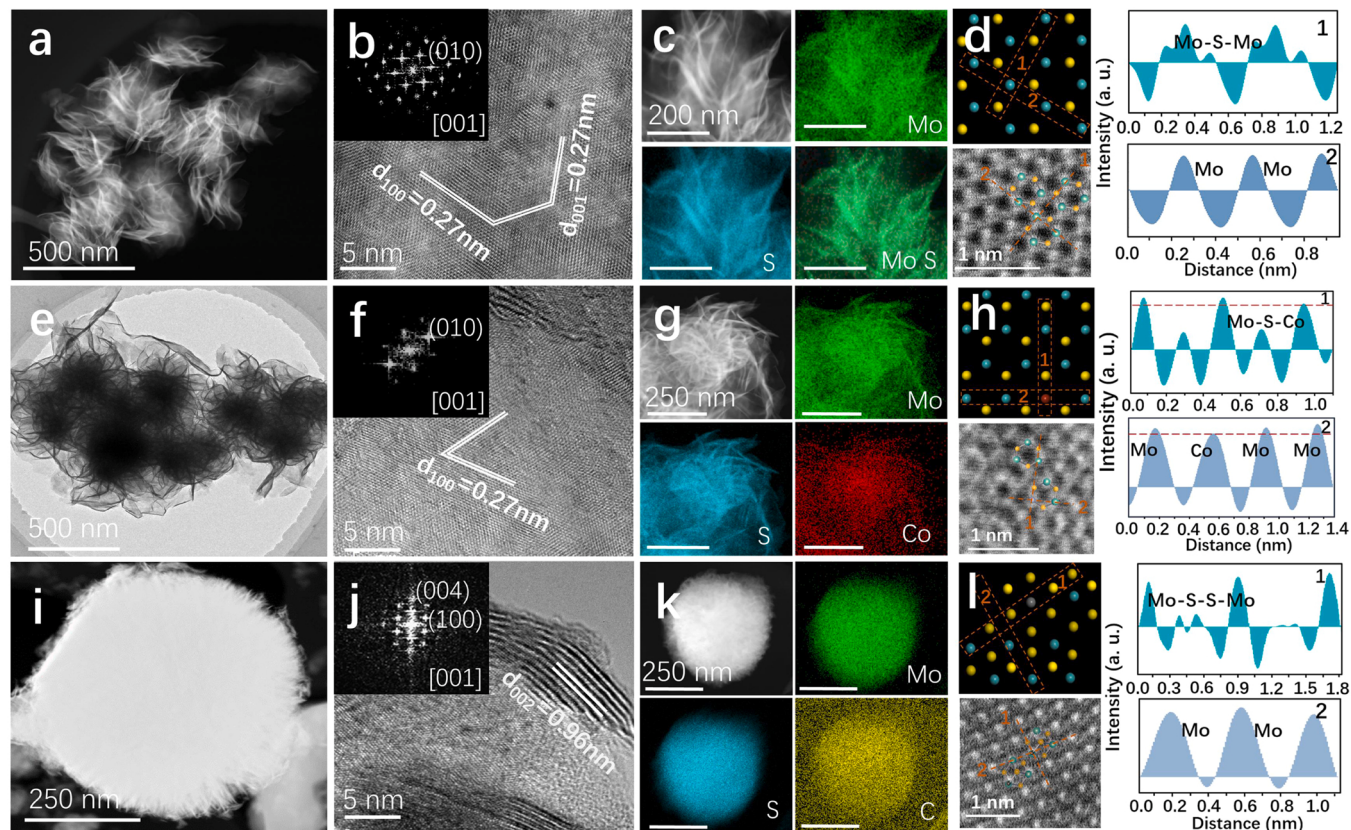


Fig. 2. Characterization of the MoS₂, Co-MoS₂, and C_{ia}-MoS₂ catalysts. (a, e, i) HRTEM images, (b, f, j) HRTEM lattice fringes; the top-left illustration shows the SAED pattern, (c, g, k) HAADF images and EDS elemental mapping images, (d, h, l) Theoretical model, HAADF-STEM image and the corresponding line intensity analysis.

Meanwhile, the insertion of C_{ia} leads to broadening of the MoS₂ (004) planes and poor crystallinity (Fig. 2j), which are characteristics of metallic 1 T-MoS₂ [29,30]. It is speculated that the C_{ia}-induced strain can be released by sliding the surface S framework, and thereby make the 1 T-MoS₂ structure more thermodynamically stable [31]. Furthermore, the atomic arrangement was confirmed by line intensity profile analysis along the orange dashed line in the theoretical model. The magnified HAADF-STEM images in Fig. 2h show that the embedded Co atoms have lower contrast than nearby Mo atoms. For C_{ia}-MoS₂, it is difficult to directly observe C_{ia} due to the electron scattering ability close to that of S, whereas, the obvious widening of lattice fringes (Fig. 2j) can strongly prove the 1 T structure induced by C_{ia}.

3.2. Electronic configuration and coordination structure analysis

To decipher the modulation mechanisms of dopants on the electronic configuration of MoS₂, DFT calculations were performed. The calculated charge density differences and Bader charge revealed the reconfiguration of charge in the MoS₂ system after C_{ia} or Co atomic doping. Fig. 3a displays distinct local electron aggregation around C_{ia}, indicating an influx of electrons from the surrounding environment, which is attributed to the loss of electrons in adjacent S and Mo driven by the high electronegativity of C_{ia}. Bader charge analysis of C_{ia}-MoS₂ (Fig. S7) verified that the C_{ia} possesses -0.51 valence, while the valence of both Mo and S nearby C_{ia} was slightly increased. It confirmed the positive shift of the C_{ia}-Mo-S peak in the XPS analysis, likewise, S₂₋ ligands probably originated from the mutual hybridization of metastable S atoms due to their significant electron outflow. However, such strong electron interactions were not distinct in the Co-MoS₂ system, as a lack of visible changes in electron distribution around MoS₂ (Fig. 3b and Fig. S8). Next, electron localization functions (ELFs) were conducted to demonstrate bonding and the distribution landscape of free charge. Apparently, the electron outflow of S triggers significant electronic

localization between S-C_{ia} (Fig. 3c and Fig. S9), implying that the unpaired electrons flooded in the surface S layer can easily transfer to the H₂O molecules and thereby smooth the water-dissociation process [32]. On the other hand, the relative delocalization of electrons between C_{ia}-Mo indicates the existence of covalent bonds, contributing to the stabilization of the C_{ia}-MoS₂ system. In contrast, Co-S exhibits stronger covalent bond properties and is unable to alleviate the drastic electron localization of the surface S layer which is caused by paired electrons (Fig. S10).

To obtain experimental evidence for the evolution of the coordination structure in MoS₂ anchored by C_{ia} or Co, X-ray absorption near-edge structure (XANES) and extended X-ray absorption fine structure (EXAFS) analyses were implemented. Fig. 3d shows the Mo K-edge XANES spectra of MoS₂, Co-MoS₂, C_{ia}-MoS₂, and Mo foil; the absorption edge and white line intensity were lowest for Mo foil. The magnified insets show the increased absorption edge and white line intensity of C_{ia}-MoS₂, indicating the transition of Mo to a higher oxidation state, consistent with the above analysis. Furthermore, Co doping decreases the intensity of the white line due to its lower electronegativity than Mo [33]. The corresponding Mo K-edge EXAFS oscillation functions $k^2\chi(k)$ are presented in Fig. S11. Apparently, the as-synthesized MoS₂ catalysts possess similar oscillation structures in the absence of other compounds. Fig. 3e illustrates the Mo K-edge after the $k^3[\chi(k)]$ -weighted Fourier transform in R-space. The major peaks around 1.9 and 2.9 Å were assigned to the Mo-S and Mo-Mo scattering in MoS₂, and a noticeable peak located at a lower position of 1.6 Å was assigned to the C_{ia}-Mo scattering contribution [34]. Meanwhile, Co-MoS₂ was mainly exposed by the Co-S coordination path since Co atoms were confined in the MoS₂ lattice by replacing Mo atoms, so Mo-Co scattering was not observed in the Mo K-edge [35].

To more definitively illustrate the affection for coordination structure in modified MoS₂, wavelet transform (WT) was performed on the Mo K-edge EXAFS oscillation (Fig. 3f and Fig. S12). Two intensity

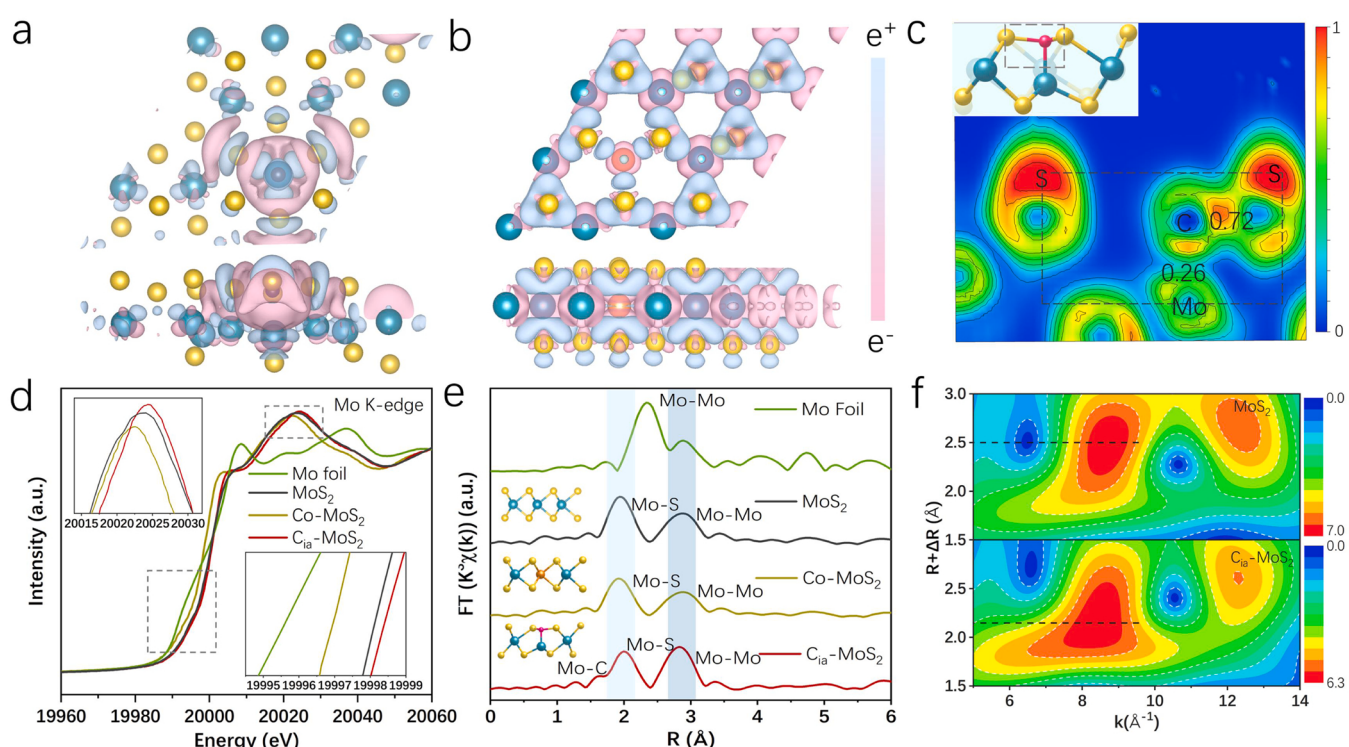


Fig. 3. The electronic structure and coordination structure analysis of the MoS₂, Co-MoS₂, and C_{ia}-MoS₂ catalysts. (a, b) Calculated difference charge density of C_{ia}-MoS₂ and deformation charge density of Co-MoS₂. The blue and pink regions indicate an increase and decrease in charge density, respectively, (c) Calculated electron localization function of C_{ia}-MoS₂; inset is a schematic diagram of the tangent plane, (d) Mo K-edge XANES spectra; insets are magnified absorption edge and the white line intensity, (e) FT-EXAFS spectrum for the Mo K-edge, (f) WT-EXAFS spectrum for the Mo K-edge.

maxima are associated with Mo-S and Mo-Mo paths. The downward-moved prominent peak in Fig. 3 f can be ascribed to the electronic structure perturbation on Mo by newly formed C_{ia}-Mo coordination with a coordination number of 1 [36], which, is based on the fitted EXAFS data (Table S3). Additionally, the short length of the C_{ia}-Mo bond confirmed that the C atoms were pulled into the sublayer of MoS₂. In accordance with the positive shift of the S²⁻ peaks, atomic C was proved to be interstitially coordinated, as expected, since the occupation of the S site by C has been reported to cause an apparent negative shift in the S 2p binding energy [35–37]. Notably, the bond length differences in the R space, WT, and fitting results were attributed to unavoidable phase-uncorrection. In addition to the coordination structure, the geometric distortion of modified MoS₂ catalysts was also revealed by the radial distribution of the Fourier-transformed EXAFS spectrum [38]. As shown in Fig. S13, the C_{ia}-MoS₂ presents the largest ratio of the Mo-Mo path to the Mo-S path scattering increment, demonstrating the most drastic structural distortion compared to pristine MoS₂, followed by that of Co-MoS₂. The XAFS results clearly revealed that the irreversible local coordination reconstruction was a direct structural response to the incorporation of C_{ia} into the lattice interstice, despite the similar original

structure.

3.3. HER performance analysis

The electrocatalytic properties of these MoS₂ catalysts towards the HER were evaluated in a 0.5 M H₂SO₄ solution (see details in Methods). C_{ia}-MoS₂ allows the highest HER activity, with the lowest overpotential of 87 mV (vs. RHE) (Fig. 4a), much better than Co-MoS₂ and MoS₂. To quantitate the HER catalytic activity, the turnover frequency (TOF) was calculated to disclose the intrinsic activity of a single active site (Fig. 4b). The TOF value of C_{ia}-MoS₂ at an overpotential of ~350 mV (vs. RHE) was 65.97 s⁻¹, significantly higher than that of Co-MoS₂ (9.8 s⁻¹) and MoS₂ (1.2 s⁻¹) (Fig. S14). It is speculated that C_{ia} stimulates the chemical reactivity of the surface S framework and leads to such a remarkable breakthrough. Comparatively, the unpaired electrons in the d orbital of the Co contribute a specific concentration of electrons but are unable to stimulate more active sites. The double layer capacitance per unit geometric surface area (C_{dl}) (Fig. 4c) determined from the cyclic voltammetry (CV) curves (Fig. S15) was used to assess the electrochemical active surface area (ECSA). The ECSA of C_{ia}-MoS₂ was

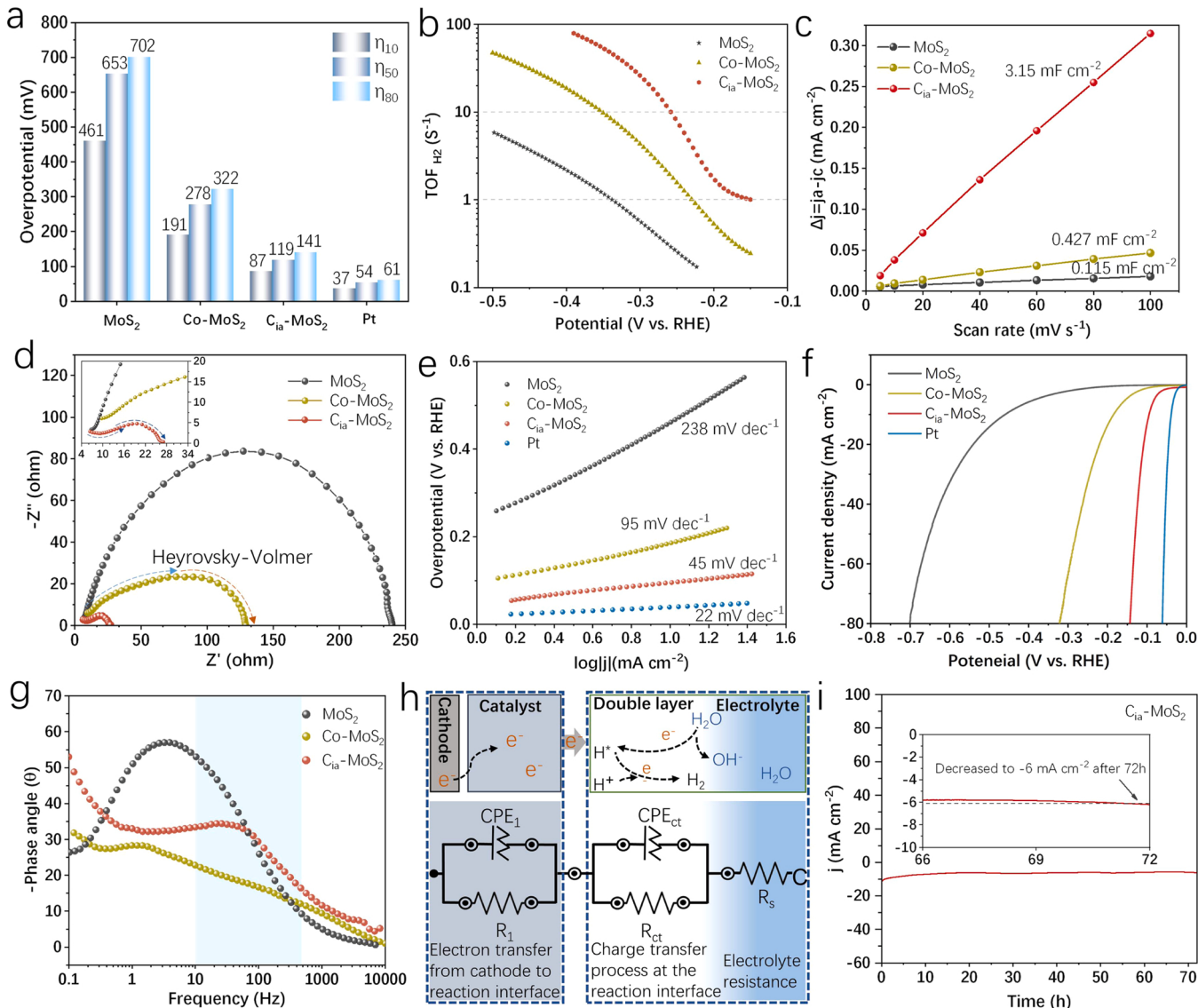


Fig. 4. HER measurements of MoS₂, Co-MoS₂, and C_{ia}-MoS₂ catalysts. (a) Overpotentials for achieving a current density of 10, 50, and 80 mA cm⁻², (b) Comparative TOF values, (c) Measured capacitive currents plotted, (d) EIS Nyquist plots, where the inset is a magnified image of the high-frequency region, (e) Tafel plots, (f) LSV curves, (g) Bode plots, (h) Equivalent circuit fitting of EIS data, (i) Stability testing of C_{ia}-MoS₂ catalysts at a constant voltage of ~0.085 V for 72 h.

9.89 cm²_{ECFA}, which is approximately 7.4 and 27.5 times better than those of Co-MoS₂ and MoS₂, respectively (Table S4). Furthermore, electrochemical impedance spectroscopy (EIS) at a constant open circuit potential (Fig. 4d) indicated that C_{ia}-MoS₂ possessed the smallest charge-transfer resistance (R_{ct}) value of 20.2 Ω, which is 1/11 and 1/6 those of MoS₂ and Co-MoS₂, respectively.

To gain a detailed understanding of the HER mechanism of the as-synthesized catalysts, Tafel slopes, Nyquist plots, Bode plots, and corresponding equivalent circuits were analysed (Fig. 4d-h). The HER mechanism under acidic conditions can be divided into three fundamental steps: Volmer ($\text{H}_3\text{O}^+ + \text{e}^- \rightarrow \text{H}_2\text{O} + \text{H}^+$), Heyrovsky ($\text{H}_3\text{O}^+ + \text{H}^* + \text{e}^- \rightarrow \text{H}_2\text{O} + \text{H}_2$), and Tafel ($2\text{H}^* \rightarrow 2\text{M} + \text{H}_2$) steps [39]. Due to the specific relaxation time, the Volmer and Herovsky steps are highly related to the low-frequency and intermediate-frequency regions of the Bode plots [40,41], respectively. The Tafel step cannot be identified by EIS since there is no electron transfer. By considering the Tafel slope values of the HER for the as-synthesized MoS₂ samples, the rate-determining step (RDS) and HER mechanism can be identified. According to the Tafel slope formula, $b = (2.303RT)/[(a^* + n)F]$ (a^* : number of electron transfers for the RDS and n : number of electron transfers before the RDS), the Tafel slope of MoS₂ (238 mV dec⁻¹) evinces that pristine MoS₂ follows a traditional Volmer mechanism ($a^*=0.5$ and $n=0$), which is limited by sluggish water dissociation. For Co-MoS₂, the Tafel slope of 95 mV dec⁻¹ demonstrated a Volmer-Heyrovsky mechanism with an accelerated water-splitting process; however, it was limited by the Heyrovsky step ($a^*=0.5$ and $n=0.15$). The lowest Tafel slope of 45 mV dec⁻¹ indicated that C_{ia}-MoS₂ also obeys a Volmer-Heyrovsky mechanism ($a^*=0.5$ and $n=1$). With the significantly reduced R_{ct}, water dissociation was very efficient in the C_{ia}-MoS₂ catalyst with an improved Heyrovsky step, resulting in better HER activity than in the other catalysts. Based on the analysis

above, the equivalent circuit was determined to consist of three parallel processes (Fig. 4h): interfacial resistance resulting from electron transport between the substrate and active surface layer (CPE₁ and R₁), charge transfer resistance at the reaction interface (CPE_{ct} and R_{ct}), and electrolyte resistance (R_s). Therefore, R_s was calculated from the real axis intercept of the Nyquist plots in the high-frequency region that was proven to exist in the diffuse double layer (DDL) [41]. In addition, the intercept of the Nyquist plots in the low-frequency region was used to find the sum of R_{ct} and R_s; thus, R_{ct} was obtained from the diameter of the semicircle (Table S5). The long-term stabilities of C_{ia}-MoS₂ (Fig. 4i) and other catalysts were examined using chronoamperometry (i-t) at constant voltages (Fig. S16). After 72 h continuously generating H₂ of C_{ia}-MoS₂, only negligible decay of about 5 mV was observed in high current density region (Fig. S17). Applicable XRD, Raman, XPS spectrums, as well as HRTEM images, reveal that as-synthesized MoS₂ catalysts retain their morphology and structure after long-term HER stability testing (Figs. S18-S21). On the basis of the above experimental analysis, the extraordinary HER performance of C_{ia}-MoS₂ was attributed to the formed conductive structure and its superb electrical properties. First, the metallic properties of the 1 T phase C_{ia}-MoS₂ lead to excellent current efficiency. Second, the vertical nanosheets distributed on radial spherical particles fully exposed more active edges. Finally, the reconfigured charge landscape and coordination structures of C_{ia}-MoS₂ led to the best hydrogen evolution behavior and long-lasting durability over 72 h. The outstanding overpotential (87 mV at 10 mA cm⁻²) and Tafel slope (45 mV dec⁻¹) correspond to the highest performance among previously reported heteroatom-doped MoS₂ in 0.5 M H₂SO₄ electrolyte (Fig. S22 and see Table S6 for details).

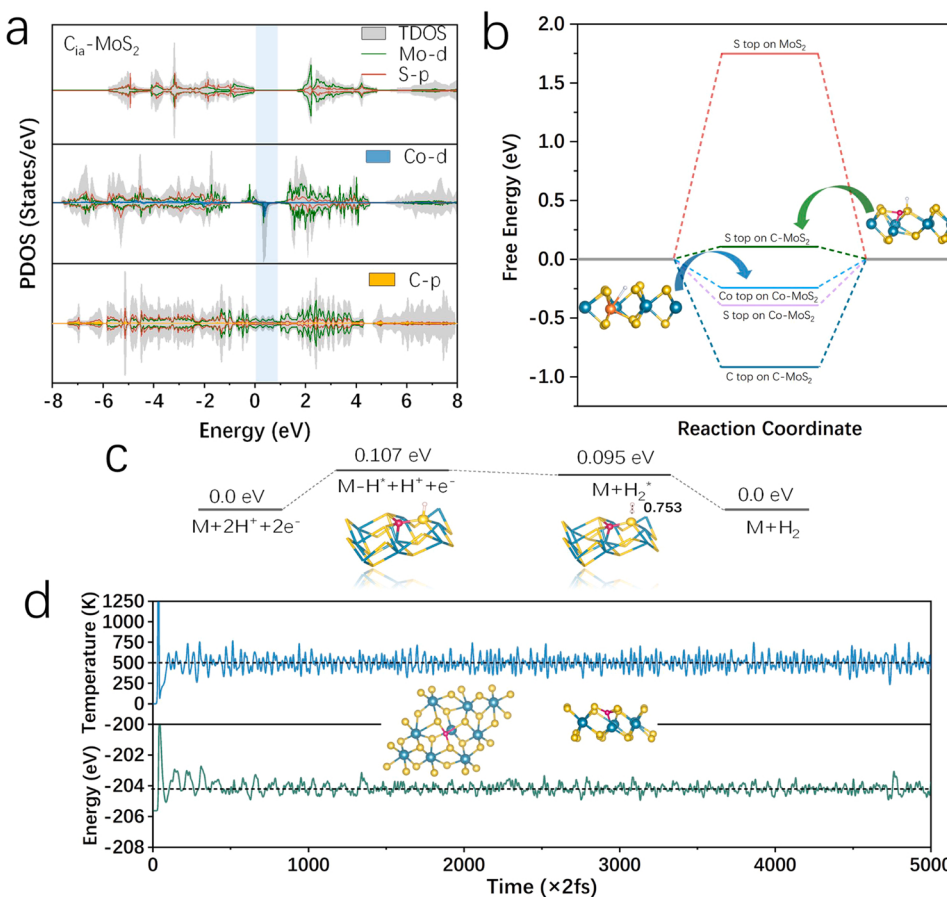


Fig. 5. (a) Calculated TDOS and PDOS analysis of MoS₂, Co-MoS₂, and C_{ia}-MoS₂, (b) Calculated hydrogen adsorption free energy at different sites of MoS₂, Co-MoS₂, and C_{ia}-MoS₂; insets are the best hydrogen adsorption modes on C_{ia}-MoS₂ and Co-MoS₂ catalysts, (c) Reaction pathway of HER on C_{ia}-MoS₂ according to the Volmer-Heyrovsky mechanism. Blue, yellow, pink, and white indicate Mo, S, C, and H atoms, respectively, (d) The temperature and energy fluctuations of C_{ia}-MoS₂ during 10 ps of AIMD simulation at T = 500 K; insets are the top and side views of C_{ia}-MoS₂ after AIMD simulation.

3.4. The intrinsic HER activity mechanism

Next, the DOS was calculated to disclose the changes in the energy band property of $\text{C}_{\text{ia}}\text{-MoS}_2$ relative to Co-MoS₂ and MoS₂, thus providing insight into the HER activity modulation induced by dopants in MoS₂. As shown in Fig. 5a, the total density of states (TDOS) of $\text{C}_{\text{ia}}\text{-MoS}_2$ and Co-MoS₂ exhibit metallic and semimetallic properties. The energy level splitting of the projected DOS (PDOS) of the S and Mo orbitals was further implemented to describe the dynamics (Fig. S23). Specifically, the unpaired electrons (4S2 3d7) donated by Co cause the PDOS of Mo ($4d_z^2$, $4d_{xy}$, and $4d_{x^2-y^2}^2$) and S ($3p_x$, $3p_y$, and $3p_z$) orbital obviously polarized between the band gaps (Fig. S24), while the $4d_{xz}$ and $4d_{yz}$ orbitals maintain a wide band gap because of their strong interactions with S [42,43]. For $\text{C}_{\text{ia}}\text{-MoS}_2$, as shown in Fig. S25, the moderate energy level splitting of Mo 4d and S 3p induced by the coordination structure transition promotes charge transfer. Through the hybridization of C 2p orbitals, electrons of S and Mo are allowed to flux to C_{ia} , which gives rise to a stronger interaction between S and H* [34,44].

We evaluated the H* adsorption/desorption ability for the different sites on these catalysts based on the DFT calculated free energy (ΔG_{H^*}) (Fig. 5b). Atomic Co introduced a new hydrogen adsorption site on its top position, with ΔG_{H^*} of -0.243 eV, subsequently, the adsorbed hydrogen (H*) moved to the tilted top site towards the adjacent S atom due to the electrostatic interaction [27]. Clearly, this strengthened the adsorption of hydrogen; however, it is inevitably overbound with H*. Moreover, a stable hydrogen adsorption site on the adjacent S-top was induced by C_{ia} , with ΔG_{H^*} of 0.107 eV, indicating the most favorable HER activity. Furthermore, as shown in Fig. S26, the reaction pathway on $\text{C}_{\text{ia}}\text{-MoS}_2$ is determined to be the most energetically favored by examining HER process on those catalysts. A detailed hydrogen generation schematic diagram on $\text{C}_{\text{ia}}\text{-MoS}_2$ is given in Fig. 5c. As observed in our experiment, a free H atom is first adsorbed on the catalyst surface with extremely low energy, later, another free H combines with the adsorbed H atom to form a H₂ molecule. The calculated H₂ desorption energy of -0.095 eV demonstrates fast HER kinetic of $\text{C}_{\text{ia}}\text{-MoS}_2$. Finally, the thermodynamic stability of the $\text{C}_{\text{ia}}\text{-MoS}_2$ structure was evaluated by ab-initio molecular dynamics (AIMD) simulation using the Nosé-Hoover heat bath scheme at 500 K for 10 ps with a time step of 2 fs. As shown in Fig. 5d, at a temperature of 500 K, the energy and temperature oscillate near the equilibrium state, indicating the high thermodynamic stability of the $\text{C}_{\text{ia}}\text{-MoS}_2$ geometry. In brief, the optimal hydrogen adsorption behavior of $\text{C}_{\text{ia}}\text{-MoS}_2$ was attributed to energy-level splitting properties and the unsaturated electronic structure of the surface S framework. First, the strong $\text{C}_{\text{ia}}\text{-Mo}$ bonding stabilizes the conductive 1 T phase and contributes to efficient charge transport. Second, the introduction of C 2p orbitals modulates the interaction of the surface S with H*, thus overcoming the sluggish Volmer process. Third, hydrogen exhibited strong or even excessive adsorption on Co sites, which served as the active center. In contrast, C_{ia} with high chemical potential was calculated to be inert; it encourages the adjacent S to absorb H* moderately by reconfiguring the charge landscape.

4. Conclusions

MoS₂ is an attractive electrocatalyst for hydrogen evolution due to its tunable lamellar structure and potential electrical properties. By confining C_{ia} in the subsurface interstice, the MoS₂ catalyst is more applicable toward HER in terms of surface hydrogen affinity, electronic mobility, intrinsic activity, and thermodynamic stability. DFT calculation confirmed that the moderate energy level splitting of S enables a thermally neutral ΔG_{H^*} on the $\text{C}_{\text{ia}}\text{-MoS}_2$ basal plane, leading to the most favorable chemisorption energy for hydrogen species. The unsaturated electronic structure modulated by C_{ia} accelerates the water-splitting process (Volmer step), giving the lowest Tafel slope of 45 mV dec^{-1} while the counterpart of Pt is 22 mV dec^{-1} . Moreover, the firm $\text{C}_{\text{ia}}\text{-Mo}$

bond driven by the high chemical potential makes 1 T $\text{C}_{\text{ia}}\text{-MoS}_2$ maintain a thermodynamically stable structure during the HER catalyze lasting over 72 h. Undoubtedly, our work disclosed the catalytic mechanisms of C_{ia} in boosting MoS₂ for hydrogen evolution and revealed the advantages of interstitial atom engineering in building the structural diversity of catalysts.

CRediT authorship contribution statement

Qingqing Zhou: Conceptualization, Software, Formal analysis, Writing – original draft, Writing – review & editing. **Zhongyuan Wang:** Methodology, Validation. **Huadong Yuan:** Methodology, Investigation, Software. **Jiade Wang:** Supervision, Project administration, Funding acquisition. **Hao Hu:** Validation, Writing – review & editing.

Declaration of Competing Interest

The authors declare that they have no known competing financial interests or personal relationships that could have appeared to influence the work reported in this paper.

Data availability

The authors do not have permission to share data. No data was used for the research described in the article.

Acknowledgements

The authors are grateful to the financial support from the National Natural Science Foundation of China (No. 52270110) and the Special Support Plan for High Level Talents in Zhejiang Province (No. 2017R52018).

Appendix A. Supporting information

The Supporting Information is available free of charge from the corresponding author upon reasonable request. Detailed descriptions in the experimental section, supplementary microscopy images, material characterization, electrochemical evaluation, and DFT calculation are in Supporting Information. Supplementary data associated with this article can be found in the online version at doi:10.1016/j.apcatb.2023.122750

References

- [1] G. Glenk, S. Reichelstein, Economics of converting renewable power to hydrogen, *Nat. Energy* 4 (2019) 216.
- [2] H.M. Liu, R.K. Xie, Y.T. Luo, Z.C. Cui, Q.M. Yu, Z.Q. Gao, Z.Y. Zhang, F.N. Yang, X. Kang, S.Y. Ge, S.H. Li, X.F. Gao, G.L. Chai, L. Liu, B.L. Liu, Dual interfacial engineering of a Chevrel phase electrode material for stable hydrogen evolution at 2500 mA cm^{-2} , *Nat. Commun.* 13 (2022) 6382.
- [3] H.J. Yin, S.L. Zhao, K. Zhao, A. Muqsite, H.J. Tang, L. Chang, H.J. Zhao, Y. Gao, Z. Y. Tang, Ultrathin platinum nanowires grown on single-layered nickel hydroxide with high hydrogen evolution activity, *Nat. Commun.* 6 (2015) 6430.
- [4] L.A. King, M.A. Hubert, C. Capuano, J. Manco, N. Danilovic, E. Valle, T. R. Hellstern, K. Ayers, T.F. Jaramillo, A non-precious metal hydrogen catalyst in a commercial polymer electrolyte membrane electrolyser, *Nat. Nanotechnol.* 14 (2019) 1071.
- [5] T.F. Jaramillo, K.P. Jorgensen, J. Bonde, J.H. Nielsen, S. Horch, I. Chorkendorff, Identification of active edge sites for electrochemical H₂ evolution from MoS₂ nanocatalysts, *Science* 317 (2007) 100.
- [6] Y. Zhou, J. Zhang, E. Song, J.H. Lin, J.D. Zhou, K. Suenaga, W. Zhou, Z. Liu, J. J. Liu, J. Lou, H.J. Fan, Enhanced performance of in-plane transition metal dichalcogenides monolayers by configuring local atomic structures, *Nat. Commun.* 11 (2020) 2253.
- [7] C. Tsai, K. Chan, J.K. Norskov, F.A. Pedersen, Theoretical insights into the hydrogen evolution activity of layered transition metal dichalcogenides, *Surf. Sci.* 640 (2015) 133.
- [8] L.J. Zhou, M.Y. Li, W. Wang, C. Wang, H.P. Yang, Y. Cao, Edge engineering in chemically active two-dimensional materials, *Nano Res.* 15 (2022) 9890.

- [9] B. Hinnemann, P.G. Moses, J. Bonde, K.P. Jorgensen, J.H. Nielsen, S. Horch, I. Chorkendorff, J.K. Norskov, Biomimetic hydrogen evolution: MoS₂ nanoparticles as catalyst for hydrogen evolution, *J. Am. Chem. Soc.* 127 (2005) 5308.
- [10] C. Tsai, K. Chan, F.A. Pedersen, J.K. Norskov, Active edge sites in MoSe₂ and WSe₂ catalysts for the hydrogen evolution reaction: a density functional study, *Phys. Chem. Chem. Phys.* 16 (2014) 13156.
- [11] C. Tsai, H. Li, S. Park, J. Park, F.A. Pedersen, Electrochemical generation of sulfur vacancies in the basal plane of MoS₂ for hydrogen evolution, *Nat. Commun.* 8 (2017) 15113.
- [12] H.T. Wang, C. Tsai, D.S. Kong, K. Chan, F.A. Pedersen, J.K. Norskov, Y. Cui, Transition-metal doped edge sites in vertically aligned MoS₂ catalysts for enhanced hydrogen evolution, *Nano Res.* 8 (2015) 566.
- [13] W.S. Chen, J.J. Gu, Y.P. Du, F. Song, F.X. Bu, J.H. Li, Y. Yuan, R.C. Luo, Q.L. Liu, D. Zhang, Achieving rich and active alkaline hydrogen evolution heterostructures via interface engineering on 2D 1T-MoS₂ quantum sheets, *Adv. Funct. Mater.* 30 (2020), 2000551.
- [14] L. Ries, E. Petit, T. Michel, C.C. Diogo, C. Gervais, C. Salameh, M. Bechelany, S. Balme, P. Miele, N. Onofrio, D. Voiry, Enhanced sieving from exfoliated MoS₂ membranes via covalent functionalization, *Nat. Mater.* 18 (2019) 1112.
- [15] X.Y. Chen, Z. Wang, Y. Wei, X. Zhang, Q. Zhang, L. Gu, L. Zhang, N. Yang, R. Yu, High phase-purity 1T-MoS₂ ultrathin nanosheets by a spatially confined template, *Angew. Chem.* 131 (2019) 17785.
- [16] T.H.M. Lau, X.W. Lu, J. Kulhavy, S. Wu, L.L. Lu, T. Wu, R. Kato, J.S. Foord, Y. L. Soo, K. Suenaga, S.C.E. Tsang, Transition metal atom doping of the basal plane of MoS₂ monolayer nanosheets for electrochemical hydrogen evolution, *Chem. Sci.* 9 (2018) 4769.
- [17] Y. Li, Q.F. Gu, B. Johannessen, Z. Zheng, G. Li, Y.T. Luo, Z.Y. Zhang, Q. Zhang, H. N. Fan, W.B. Luo, B.L. Liu, S.X. Duo, H.K. Liu, Synergistic Pt doping and phase conversion engineering in two-dimensional MoS₂ for efficient hydrogen evolution, *Nano Energy* 84 (2021), 105898.
- [18] Y. Sun, Y. Zang, W. Tian, X. Yu, J. Qi, L. Chen, X. Liu, H. Qiu, Plasma-induced large-area N, Pt-doping and phase engineering of MoS₂ nanosheets for alkaline hydrogen evolution, *Energy Environ. Sci.* 15 (2022) 1201–1210.
- [19] I. Show, S. Samireddi, Y.C. Chang, R. Putikam, P.H. Chang, A. Sabbah, F.Y. Fu, W. F. Chen, C.L. Wu, T.Y. Yu, Carbon-doped SnS₂ nanostructure as a high-efficiency solar fuel catalyst under visible light, *Nat. Commun.* 9 (2018) 169.
- [20] K. Zhang, Y.C. He, R.Y. Guo, W.C. Wang, Q. Zhan, R. Li, T.O. He, C. Wu, M.S. Jin, Interstitial carbon-doped PdMo bimetallic for high-performance oxygen reduction reaction, *ACS Energy Lett.* 7 (2022) 3329.
- [21] P. Janthon, F. vines, J. Sirijaraensre, J. Limtrakul, F. Illas, Carbon dissolution and segregation in platinum, *Catal. Sci. Technol.* 7 (2017) 807–816.
- [22] X. Wang, H. Li, H. Li, S. Lin, W. Ding, X.G. Zhu, Z.G. Sheng, H. Wang, X.B. Zhu, Y. P. Sun, 2D/2D 1T-MoS₂/Ti₃C₂ MXene heterostructure with excellent supercapacitor performance, *Adv. Funct. Mater.* 30 (2020), 1910302.
- [23] W. Ding, L. Hu, J.M. Dai, X.W. Tang, R.H. Wei, Z.G. Sheng, C.H. Liang, D.F. Shao, W.H. Song, Q.N. Liu, M.Z. Chen, X.G. Zhu, S.L. Chou, X.B. Zhu, Q.W. Chen, Y. P. Sun, S.X. Dou, Highly ambient-stable 1T-MoS₂ and 1T-WS₂ by hydrothermal synthesis under high magnetic fields, *ACS Nano* 13 (2019) 1694.
- [24] Z.J. Yin, J. Zhao, B.W. Wang, Y. Xu, Z.H. Li, X.B. Ma, Insight for the effect of bridging S₂²⁻ in molybdenum sulfide catalysts toward sulfur-resistant methanation, *Appl. Surf. Sci.* 471 (2019) 670.
- [25] B. Gao, X.Y. Du, Y.H. Li, S.J. Ding, C.H. Xiao, Z.X. Song, Deep phase transition of MoS₂ for excellent hydrogen evolution reaction by a facile C-doping strategy, *ACS Appl. Mater. Interface* 12 (2020) 877.
- [26] Z. Wang, H. Luo, R. Lin, H. Lei, Y. Yuan, Z. Zhu, X. Li, W. Mai, Theoretical calculation guided electrocatalysts design: nitrogen saturated porous Mo2C nanostructures for hydrogen production, *Appl. Catal. B Environ.* 257 (2019), 117891.
- [27] K. Qi, X.Q. Cui, L. Gu, S.S. Yu, X.F. Fan, M.C. Luo, S. Xu, N.B. Li, L.R. Zheng, Q. H. Zhang, J.Y. Ma, Y. Gong, F. Lv, K. Wang, H.H. Huang, W. Zhang, S.J. Guo, W. T. Zheng, P. Liu, Single-atom cobalt array bound to distorted 1T MoS₂ with ensemble effect for hydrogen evolution catalysis, *Nat. Commun.* 10 (2019) 5231.
- [28] Z.Y. Luo, Y., X. Ouyang, H. Zhang, M.L. Xiao, J.J. Ge, Z. Jiang, J.L. Wang, D. M. Tang, X.Z. Cao, C.P. Liu, W. Xing, Chemically activating MoS₂ via spontaneous atomic palladium interfacial doping towards efficient hydrogen evolution, *Nat. Commun.* 9 (2018) 2120.
- [29] L. Yang, A. Mukhopadhyay, Y.C. Jiao, J. Hamel, M. Benamara, Y.J. Xing, H.L. Zhu, Aligned and stable metallic MoS₂ on plasma-treated mass transfer channels for the hydrogen evolution reaction, *J. Mater. Chem. A* 5 (2017) 25359.
- [30] R.Q. Liu, T. Guo, H. Fei, Z.Z. Wu, D.Z. Wang, F.Y. Liu, Highly efficient electrocatalytic N₂ reduction to ammonia over metallic 1T phase of MoS₂ enabled by active sites separation mechanism, *Adv. Sci.* 9 (2021), 2103583.
- [31] S. Tongay, J. Zhou, C. Ataca, K. Lo, T.S. Matthews, J.B. Li, J.C. Grossman, J.Q. Wu, Thermally driven crossover from indirect toward direct bandgap in 2D semiconductors: MoSe₂ versus MoS₂, *Nano. Lett.* 12 (2012) 5576.
- [32] G.X. Lin, Q.J. Ju, X.W. Guo, W. Zhao, F.Q. Huang, Intrinsic electron localization of metastable mos₂ boosts electrocatalytic nitrogen reduction to ammonia, *Adv. Mater.* 33 (2021), 2007509.
- [33] Z.L. Zheng, L. Yu, M. Gao, X.Y. Chen, W. Zhou, C. Ma, L.H. Wu, J.F. Zhu, X. Y. Meng, J.T. Hu, Y.C. Tu, S.S. Wu, J. Mao, Z.Q. Tian, D.H. Deng, Boosting hydrogen evolution on MoS₂ via co-confining selenium in surface and cobalt in inner layer, *Nat. Commun.* 11 (2020) 3315.
- [34] Y.P. Zang, S.W. Niu, Y.S. Wu, X.S. Zheng, J.Y. Cai, J. Ye, Y.F. Xie, Y. Liu, J.B. Zhou, J.F. Zhu, X.J. Liu, G.M. Wang, Y.T. Qian, Tuning orbital orientation endows molybdenum disulfide with exceptional alkaline hydrogen evolution capability, *Nat. Commun.* 10 (2019) 1217.
- [35] Z.G. Li, C.L. Li, J.W. Chen, X. Xing, Y.Q. Wang, Y. Zhang, M.S. Yang, G.X. Zhang, Confined synthesis of MoS₂ with rich co-doped edges for enhanced hydrogen evolution performance, *J. Energy Chem.* 70 (2022) 18.
- [36] J.M. Ge, D.B. Zhang, Y. Qin, T. Dou, M.H. Jiang, F.Z. Zhang, X.D. Lei, Dual-metallic single Ru and Ni atoms decoration of MoS₂ for high-efficiency hydrogen production, *Appl. Catal. B* 298 (2021), 120557.
- [37] Y.L. Jia, Z.H. Wang, L.Y. Wang, Y. Ma, G.N. Wang, Y.H. Lin, X. Hu, K. Zhang, Awakening solar hydrogen evolution of MoS₂ in alkalescent electrolyte through doping with Co, *ChemSusChem* 12 (2019) 3336.
- [38] G.K. Han, X. Zhang, W. Liu, Q.H. Zhang, Z.Q. Wang, J. Cheng, T. Yao, L. Gu, C. Y. Du, Y.Z. Gao, G.P. Yin, Substrate strain tunes operando geometric distortion and oxygen reduction activity of CuN₂C₂ single-atom sites, *Nat. Commun.* 12 (2021) 6335.
- [39] R. Subbaraman, D. Tripkovic, D. Strmcnik, K.C. Chang, M. Uchimura, A. P. Paulikas, V. Stamenkovic, N.M. Markovic, Enhancing hydrogen evolution activity in water splitting by tailoring Li⁺-Ni(OH)₂-Pt interfaces, *Science* 344 (2011) 1256.
- [40] K. Wippermann, J. Giffin, S. Kuhri, W. Lehnert, C. Korte, The influence of water content in a proton-conducting ionic liquid on the double layer properties of the Pt/PIL interface, *Phys. Chem. Chem. Phys.* 19 (2017) 24706.
- [41] W. Chen, B.B. Wu, Y.Y. Wang, W. Zhou, Y.Y. Li, T.Y. Liu, C. Xie, L.T. Xu, S.Q. Du, M.L. Song, Deciphering the alternating synergy between interlayer Pt single-atom and NiFe layered double hydroxide for overall water splitting, *Energy Environ. Sci.* 14 (2021) 6428.
- [42] J. Xu, G.L. Shao, X. Tang, F. Lv, H.Y. Xiang, C.F. Jing, S. Liu, S. Dai, Y.G. Li, J. Luo, Z. Zhou, Frenkel-defected monolayer MoS₂ catalysts for efficient hydrogen evolution, *Nat. Commun.* 13 (2022) 2193.
- [43] Q. Chen, Y.X. Quyang, S.J. Yuan, R.Z. Li, J.L. Wang, Uniformly wetting deposition of Co atoms on MoS₂ monolayer: a promising two-dimensional robust half-metallic ferromagnet, *ACS Appl. Mater. Interfaces* 6 (2014) 16835.
- [44] D. Chen, Z.H. Pu, P.Y. Wang, R.H. Lu, W.H. Zeng, D.L. Wu, Y.T. Yao, J.W. Zhu, J. Yu, P.X. Ji, S.C. Mu, Mapping hydrogen evolution activity trends of intermetallic Pt-group silicides, *ACS Catal.* 12 (2022) 2623.